ADVANCED HEALTHCARE MATERIALS
www.advhealthmat.de

Modeling Structural Elements and Functional Responses to Lymphatic-Delivered Cues in a Murine Lymph Node on a Chip

Corrado Mazzaglia, Hafsa Munir, Iek Man Lei, Magda Gerigk, Yan Yan Shery Huang, and Jacqueline D. Shields**

Lymph nodes (LNs) are organs of the immune system, critical for maintenance of homeostasis and initiation of immune responses, yet there are few models that accurately recapitulate LN functions in vitro. To tackle this issue, an engineered murine LN (eLN) has been developed, replicating key cellular components of the mouse LN; incorporating primary murine lymphocytes, fibroblastic reticular cells, and lymphatic endothelial cells. T and B cell compartments are incorporated within the eLN that mimic LN cortex and paracortex architectures. When challenged, the eLN elicits both robust inflammatory responses and antigen-specific immune activation, showing that the system can differentiate between non specific and antigen-specific stimulation and can be monitored in real time. Beyond immune responses, this model also enables interrogation of changes in stromal cells, thus permitting investigations of all LN cellular components in homeostasis and different disease settings, such as cancer. Here, how LN behavior can be influenced by murine melanoma-derived factors is presented. In conclusion, the eLN model presents a promising platform for in vitro study of LN biology that will enhance understanding of stromal and immune responses in the murine LN, and in doing so will enable development of novel therapeutic strategies to improve LN responses in disease.

1. Introduction

The lymphatic network and lymph nodes (LNs) operate as sentinels of the immune system. Lymphatics rapidly transport tissue-derived signals to the draining LN through lymph fluid. This fluid is rich in proteins, antigen, metabolites, DNA, vesicles, excreted waste products, and pathogens.[1–3] Once in the LN, these factors are surveyed and sampled by LN resident cells primed to initiate an immune response when needed. LN functions are tightly regulated, relying on compartmentalization, cellular positioning, and cytokine gradients,[1,3–5] which can be disrupted in pathologies such as infection and cancer. In many cancers, the lymphatic system is hijacked as a route of tumor cell escape, with LNs frequently being the first site of metastasis. As in physiology, tumor-associated lymphatic vessels carry material away from tumors toward their connected LNs. Here, antitumor immune responses are initiated, but ultimately fail. This is due, in part, to the profound effect that tumor

C. Mazzaglia, J. D. Shields
MRC Cancer Unit
University of Cambridge
Cambridge CB2 0XZ, UK
E-mail: Jacqueline.shields@nottingham.ac.uk
C. Mazzaglia, M. Gerigk, Y. Y. S. Huang
The Nanoscience Centre
University of Cambridge
Cambridge CB3 0FF, UK
E-mail: yysh2@cam.ac.uk

The ORCID identification number(s) for the author(s) of this article can be found under https://doi.org/10.1002/adhm.202303720

DOI: 10.1002/adhm.202303720

H. Munir
Helmholtz Institute for Translational Oncology Mainz (HI-TRON Mainz)
55131 Mainz, Germany
H. Munir
Division of Dermal Oncoimmunology
German Cancer Research Centre (DKFZ)
69120 Heidelberg, Germany
I. M. Lei, M. Gerigk, Y. Y. S. Huang
Department of Engineering
University of Cambridge
Cambridge CB2 1PZ, UK
J. D. Shields
Translational Medical Sciences
School of Medicine
University of Nottingham Biodiscovery Institute
Nottingham NG7 2RD, UK

derived signals exert on tumor-draining LNs (TDLNs), prior to metastasis. Changes in TDLNs consist of an expansion of lymphatic sinuses (vessels surrounding the LN), remodeling of fibroblast reticular cells (FRC) and transcriptional reprogramming, which significantly alters the composition and location of resident and infiltrating immune cells.[17,30] Similar remodeling events have been observed in response to certain infection models.[6] In some cases, this remodeling is critical for stimulating immune responses in the draining LN, while in others, remodeling occurs to dampen immune responses.[6–8] LN remodeling is a critical response to immune challenge, but, in the context of cancer, this has been shown to contribute to immune dysfunction.[17,59]

LNs act as immunological meeting points for different cellular components, but how the signals received by LN constituents can influence their behavior remains unclear. However, considering dichotomous responses to infection and cancer, a more in-depth comprehension of LN function and immune cell behavior will be critical for understanding immunity, alongside developing new immunotherapies and vaccines [9]

Currently, there is a lack of in vitro platforms that accurately recapitulate the full complexity of the LN in homeostasis and disease. Traditional in vitro and in vivo models have limitations in terms of reproducibility, scalability, and complexity.[10] Therefore, there is a need for innovative platforms to mimic LN physiology in a more accurate and controlled manner. Microfluidic devices have emerged as promising tools for studying immune cell behavior and interactions in a physiologically relevant microenvironment.[11,12] In recent years, there has been increasing interest in developing microfluidic platforms to study the LN and tertiary lymphoid organs (TLOs).[13] These models offer several advantages over traditional systems, including precise control of flow rate and chemical gradients, high-throughput capabilities, and the ability to mimic the complex architecture and cell-to-cell interactions arising within the LNs. The parameters needed to build an ideal LN-on-chip include a biocompatible scaffold that allows the formation of a 3D environment, a representative hydrogel that can host different cell types including lymphoid and stromal, and a system for perfusing lymph fluid. In addition, from a functional perspective, cells in the device should be able to react to external stimuli and communicate with each other to instruct and mount an orchestrated immune response. Several independent devices have been created to model the LN on-a-chip, but most of them lack the necessary scaffold for cells to display the correct morphology and enable compartmentalization. LNs are largely composed of T and B lymphocytes, which account for 90% of total LN cellularity, stromal cell populations including FRCs, follicular dendritic cells (FDCs), blood and lymphatic endothelial cells, and infiltrating and resident myeloid populations. Critically, stromal cells have often been excluded from 3D LN microfluidic systems because they were traditionally considered to primarily be a structural component of the LN. However, in recent years much has been revealed of the importance of LN stromal cells in immunomodulation, preservation of LN function and response to pathological states, driving studies which include them in LN models.[8,14–20]

Here, we present an engineered murine LN (eLN) model that incorporates several key features of LN physiology, is assembled on a cover glass for easy imaging, and allows rapid cell retrieval for diverse post hoc analyses. The eLN is a perfusable biocompatible scaffold that contains both lymphoid and stromal cells seeded into compartment-like structures that mimic the architecture of the LN. The separation of distinct cell populations offers a platform to investigate cell migration and interactions in response to different stimuli within a tractable system, in real time. We show that cells within the eLN respond to stimuli delivered via "lymphatic" sinuses, in an antigen-specific manner that mimics the in vivo setting. The eLN also exhibits key features of the TDLN when exposed to tumor-derived factors.

2. Results

2.1. Development of a Murine LN Structure within a Hydrogel Blend

We sought to design a "hydrogel blend" device (**Figure 1A,B**). The hydrogel formulation was developed based on the criteria that it was compatible for cell survival, motility, and morphology while also having enough mechanical strength to support and maintain embedded channels.

Earlier iterations incorporated a central cell laden collagen-based compartment embedded within in a GelMA case containing murine LEC-coated channels to mimic the lymphatic sinus (Figure S1A,B, Supporting Information). With this device, lymphatic endothelial cells rapidly formed monolayers on GelMA (Figure S1C, Supporting Information), and coated the channel surface (Figure S1D, Supporting Information). Murine FRCs within the collagen compartment were viable with elongated morphology (Figure S1D, Dii, Supporting Information), in contrast to observations of cells seeded within a GelMA hydrogel which remained rounded (data not shown). However, several problems were encountered with this device. While fluorescently labeled dextran perfused via the lymphatic vessel rapidly convected through the GelMA casing, it did not penetrate into the central collagen compartment (Figure S1E,F, Supporting Information). This translated to a failure of perfused immune stimulants such as phorbol myristate acetate (PMA), to activate immune cells located within the collagen core when compared with static controls bathed in stimulant (Figure S1G, Supporting Information). Moreover, we noted that FRCs seeded within the central collagen compartment were highly contractile, causing the central collagen compartment to contract and detach from the surrounding GelMA frame.

Thus, following observations that GelMA permitted robust channel formation, but cells seeded within remained rounded, while cells in collagen gels exhibited a normal phenotype but gels contracted and channels could not be maintained, we tested different combinations of collagen and GelMA to harness the properties of both matrices in a single hydrogel blend.

Within a device aiming to incorporate multiple cell types (Figure 1A,B), this blend needed to be sufficiently robust to allow channel formation and maintenance after needle casting, while allowing cells to exhibit proper behavior. We compared combinations of 1 mg mL^{-1} col:4% GelMA, 1 mg mL^{-1} col:5% GelMA, 1 mg mL^{-1} col:7.5% GelMA, 5% GelMA, and 8% GelMA containing dense immune:FRC suspensions of ≈100 lymphocytes:1 FRC. Blends of 1 mg mL^{-1} col: 5% GelMA possessed significantly

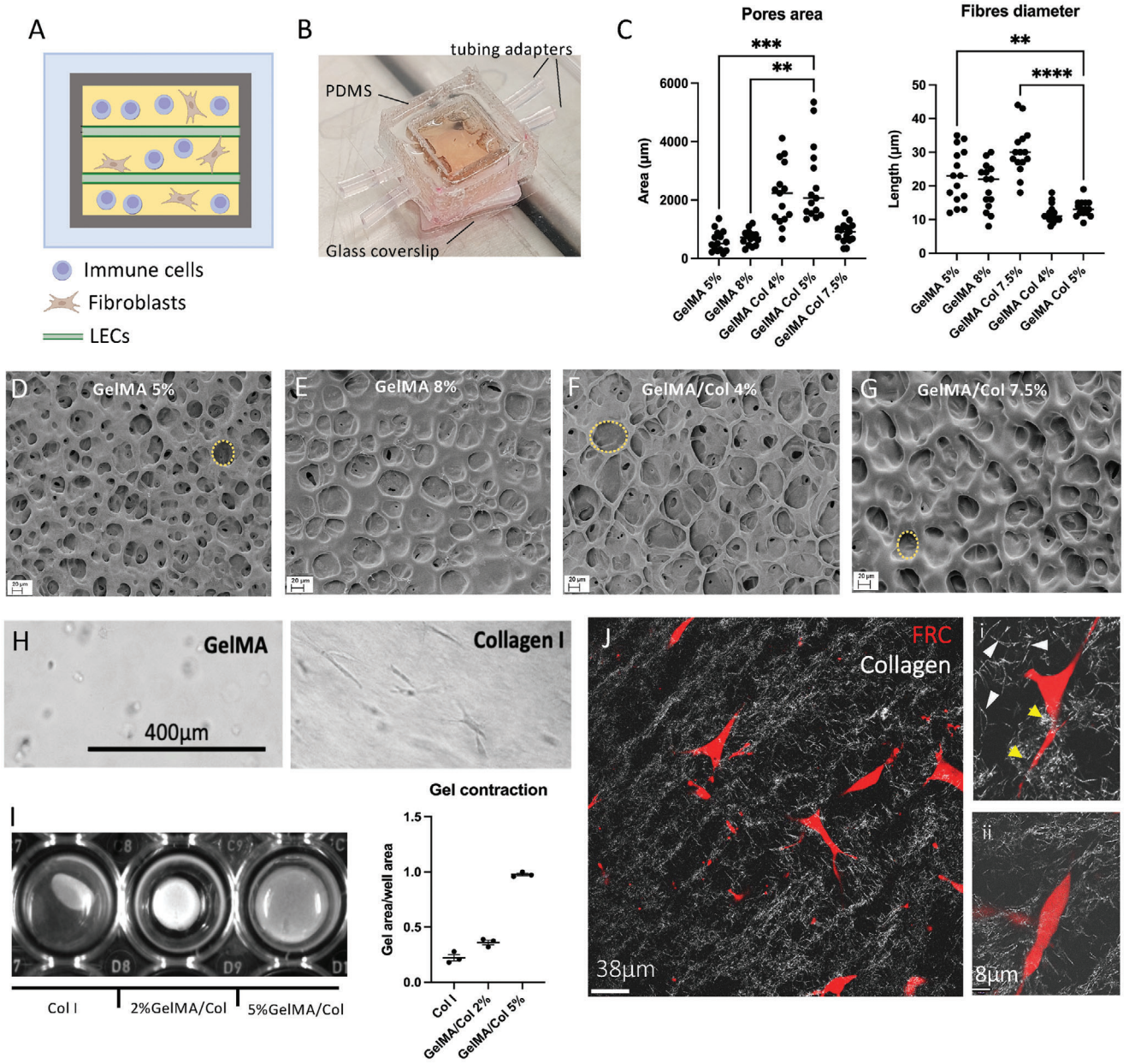

Figure 1. The hydrogel blend device supports stromal behavior without contraction. A) Schematic of the hydrogel blend eLN device containing multiple cell components. B) Final version of the PDMS case built with tubing adapters. Dimensions: 0.8 cm × 0.8 cm × 1 cm. Hydrogels were characterized with SEM imaging. C) ImageJ quantification of pore area and fiber width within the different hydrogel blends examined. Pore area measured the large opening visible [dotted yellow line in (D)]. Fiber width was measured approximately at the midpoint of each fiber. Each dot ($n = >15$) represents a single measurement taken from at least three fields of view. D–G) Representative SEM images of GelMA 5%, GelMA 8%, GelMA/Col 4%, and GelMA/Col 7.5% prepared by freeze-drying and gold coating. Scale bar = 20 µm. Images taken in the Department of Engineering Cambridge by Alex Casabuena. H) Representative bright-field images showing FRCs rounded morphology in GelMA and stretched conformation in collagen I hydrogels. I) Representative image of different fibroblast-laden hydrogel formulations (Collagen I, GelMA/collagen 2%, and GelMA/collagen 5%) depicting contraction, after 48 h of culture and quantification of gel contraction showing gel area/well area ratio, calculated manually with ImageJ. Each point ($n = 3$) represents an independent experiment. Data are mean ± SEM. J) SHG imaging of a Td Tomato-labeled TRC-laden GelMA/collagen blend cultured for 48 h showing collagen fibers (in white) and TRCs (in red), 20× magnification. Scale bar = 38 µm. i,ii) High-power micrographs (40× magnification) showing single TRCs with collagen fiber clustering. Indicated fibers (arrowhead), clusters (yellow arrow). Scale bar = 8 µm. SHG images taken with Dr Andrew Trinh. Data are mean ± SEM. One-way ANOVA and Tukey's multiple comparisons tests were conducted. ns = not significant ($p > 0.05$), *$p \leq 0.05$, **$p \leq 0.01$, ***$p \leq 0.001$, ****$p \leq 0.0001$.

larger pores and shorter fiber length compared with GelMA alone (Figure 1C–G). And, while cell-laden gels formed of collagen alone contracted by almost 80% after 24 h, 1 mg mL^{-1} col: 5% GelMA did not readily contract (Figure 1H,I). Moreover, unlike GelMA, FRCs within the hydrogel blend were able come out of a rounded state to stretch and interact with the surrounding collagen fibers (Figure 1J), akin to the cell morphologies seen in type I collagen alone (Figure 1H), and move within the ECM (Movie S1, Supporting Information). Importantly, the UV crosslinking step required to polymerize GelMA in the blended gels remained short (10 s) and did not impact cell viability compared to collagen gels.

Having identified the optimal scaffold conditions, we then sought to optimize culture conditions for the lymphocytes embedded within the eLN hydrogel. In the absence of FRCs, the viability of total $CD45^+$ immune cells in gels dropped below 10% after 48 h culture, highlighting that FRC and secreted factors are essential for immune cell maintenance in the LN. Viability was strongly boosted to over 70% by the addition of IL-4 and IL-7 (**Figure 2A**). Closer analysis of the immune compartment showed that $CD4^+$ and $CD8^+$ T cells form the bulk of the immune compartment (Figure S2A, Supporting Information) and this remained constant across conditions tested. However, FRC and cytokine support was required to maintain good T cell viability (Figure 2C,D). FRCs and cytokines also strikingly enhanced both the relative abundance (Figure S2A, Supporting Information) and survival of primary murine B cells (Figure 2B), which have previously been reported to be difficult to maintain in ex vivo models without addition of specific mitogens or genetic modifications,[21,22] boosting viability from less than 5%–40% (Figure 2B). Imaging of the cell-laden gel also indicated the existence of a close relationship between the lymphocytes and supporting FRC (Figure 2E and Figure S2B, Supporting Information). Despite equal seeding into the gel, immune cells were observed predominantly in the proximity of the FRC network (Figure S2B, Supporting Information), with clusters of immune cells seen in direct contact with FRC [Figure 2E(i,ii)] compared to FRC-poor areas [Figure 2E(iii)], indicative of either active migration toward supporting FRC, or improved survival when in proximity to FRCs and FRC-derived factors. An important modification of this device is that it operates as an open system unlike other closed-top systems. With this, we were able to consistently obtain cell yields of 1×10^6 cells, which meant that a range of post-analyses could be performed from a single experiment (Figure S2C, Supporting Information). Moreover, such modification allowed us to manipulate the 3D environment from above. Therefore, 1 mg mL^{-1} col: 5% GelMA, supplemented with IL-4 and IL-7 was selected as the optimal hydrogel for all further analyses of LN responses.

2.2. Incorporation of Lymphatic Vessels Mimicking the Subcapsular Sinus

We then tested the capacity of the hydrogel blend to support stable, perfusable channels that recapitulate the LN subcapsular sinus (SCS). Channels were cast in the hydrogel with 26G needles, using the needle-casting technique for microfluidic channel formation,[23–25] which were removed once the gel was crosslinked, creating intact cylindrical channels. These were then seeded with LECs at a concentration of 25×10^6 cells mL^{-1} to generate a fully endothelial lined and lumenized vessel (Figure 2F,G). The channels were then perfused, inducing LECs to adopt typical phenotypic and morphological features associated with flow induced shear stress, such as an elongated cell shape aligning with the direction of flow (Figure S2D–G, Supporting Information).[26] Moreover, in comparison to the earlier iteration, dextran perfused into the vessel channel now evenly convected through the entire cell-laden hydrogel, moving as an even front toward its core. Small molecular weight 3 kDa dextran transported rapidly throughout the hydrogel, passing beyond the field of view within the first 15 min of perfusion (Figure 2H left, Figure 2I). For 70 kDa dextran (the cut-off limit for what typically enters deeper into lymph nodes), a slower but equal distribution of the dextran was observed by 1 h postperfusion (at a rate of 9 µm min^{-1}) (Figure 2H,I).

2.3. Recapitulating Structural Features of the Murine LN

LNs are highly organized structures, and compartmentalization is key to immune function (**Figure 3A** and 3B). To incorporate this aspect into the system, we introduced B cell follicle and conduit-like structures. First, to form B cell follicle-like structures, LN-derived GFP^+ B cells (Figure 3A and S3A, Supporting Information) were suspended in the hydrogel at a density of 50×10^6 cells mL^{-1} with 0.4×10^6 unlabeled FRC for support. The cell-laden hydrogel solution was loaded into a syringe and kept at 4 °C for 20 min to allow thermo-gelation. Then it was injected directly into the un-crosslinked gel to form spherical droplet structures. Following this step, a suspension of T cell and Td-Tomato-labeled TRC, were manually pipetted into the gel over the follicles and needles (that create the lymphatic vessels), and the complete gel was UV photocrosslinked (Figure 3A). Cooling of the B cell solution made the printed follicles viscous enough to allow gel casting without mixing of the compartments, while both gels remained uncrosslinked. As the whole device was UV photocrosslinked simultaneously, this prevented formation of a hard interface between different cell compartments enabling cell movement across zones unlike individually polymerized compartments (Figure 3C–E and Figure S3B, Supporting Information). When polymerized separately, follicles were irregularly shaped and cells within the T cell zone would crawl along the boundary unable to cross (Figure S3C,D and Movie S2, Supporting Information).

We next generated engineered conduits (the small channels which form an essential link between the SCS and deeper LN parenchyma) out of the lymphatic channel, allowing rapid transit of small molecules such as chemokines and antigen[27–29] (**Figure 4A**). To achieve these structures, a laser capture dissection microscope was adapted to ablate narrow channels leading away from the main vessel channel into the device core (Figure 4B and Figure S4A,B, Supporting Information). Laser-carved conduits averaged 10 µm in diameter, and both single and branched structures could be achieved. Upon perfusion through the vessel, microbeads carried within the perfusate were readily detectable deep within conduits, indicative of effective transport out of the SCS toward the cell-laden compartment (Figure 4C). Moreover,

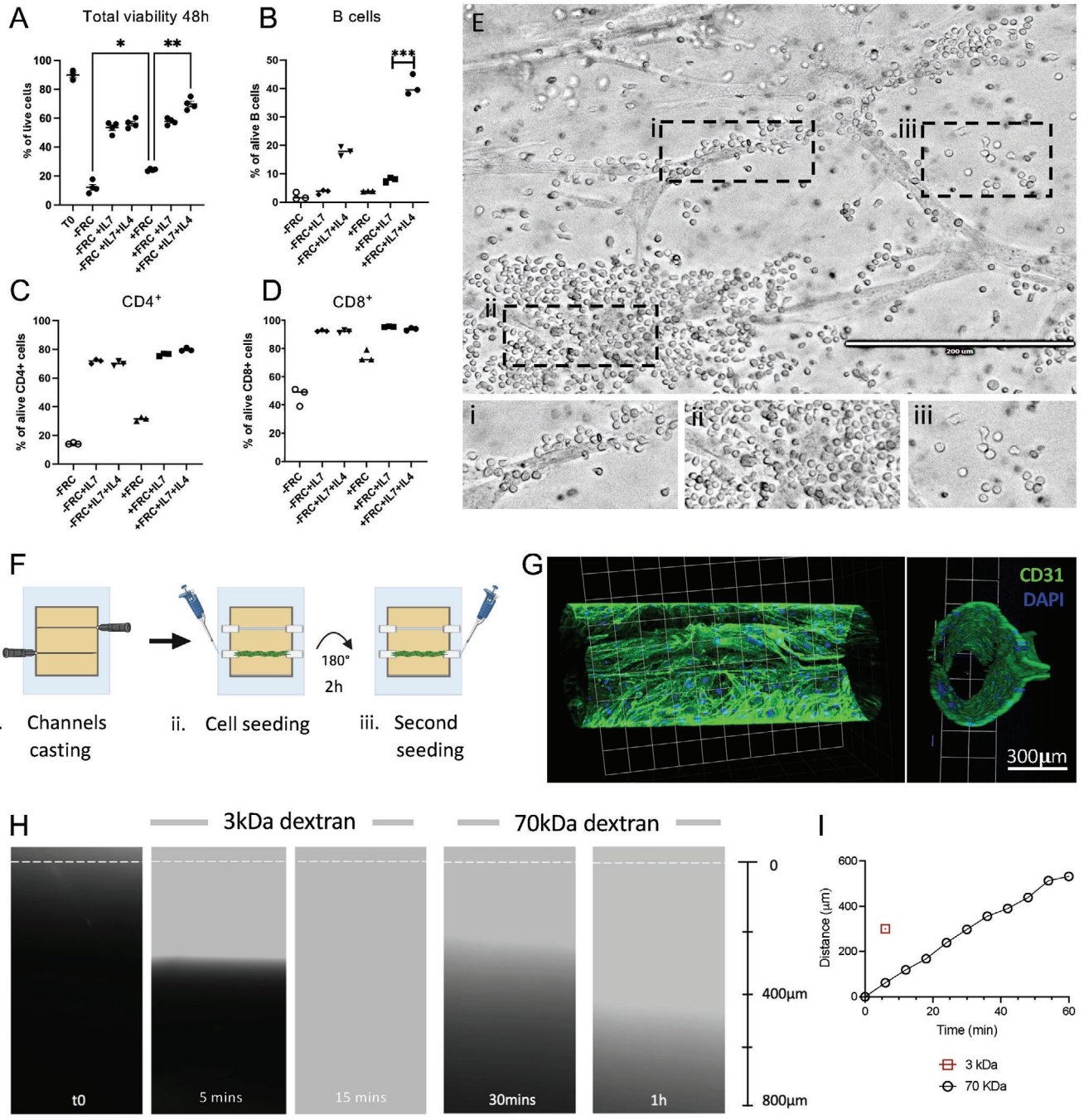

Figure 2. Optimization of culture conditions and vessel formation. A) Flow cytometry quantification of total lymphocyte viability after 48 h of culture, in comparison to viability at T0, just after extraction from a lymph node. The test was performed with or without FRCs in the hydrogel, and with or without addition of IL-7 or IL-7 and IL-4 combined to the media. Quantification of individual population viability; B) B220$^+$ B cells, C) CD4$^+$ T cells, and D) CD8$^+$ T cells. Each dot ($n = 4$) represents an independent experiment. Data are mean ± SEM. One-way ANOVA and Tukey's multiple comparisons tests were conducted. Ns = not significant ($p > 0.05$), *$p \leq 0.05$, **$p \leq 0.01$, ***$p \leq 0.001$, ****$p \leq 0.0001$. E) Representative bright-field image showing FRCs in 3D culture and preferential clustering of lymphocytes along their network. Inset: i,ii) close-ups of lymphocytes in contact with FRC fibers, and iii) fewer lymphocytes distant from FRC. F) Schematic of LECs seeding in embedded channels. G) Confocal image of a 3D embedded channel lined with LECs cultured to confluency (CD31 in green, nuclei in blue) showing its lumen. H) Images obtained with a confocal microscope shows the advancing front of 3 kDa (left; white) and 70 kDa dextran (right; white) from an acellular channel through the GelMA/collagen blend at $t = 0$, at different time points after dextran perfusion. White dotted line represents the channel edge and on the right the ruler shows distance. I) Graph showing fluorescence front distance from the channel over time (3 kDa: red; 70 kDa: black).

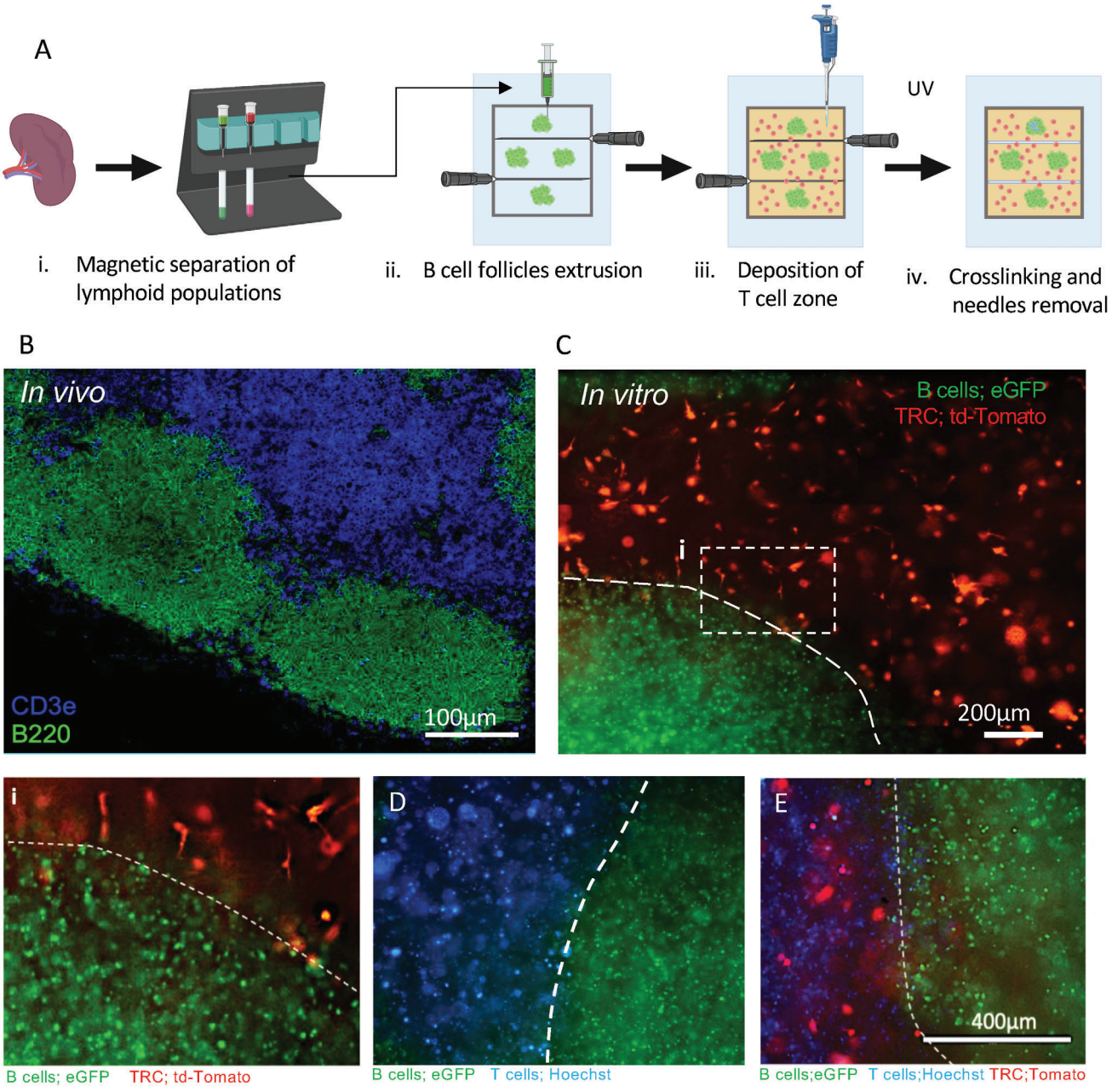

Figure 3. The eLN recapitulates cellular compartmentalization. A) Schematic of B cell follicle-like structure formation steps. B) Confocal image of a murine lymph node showing B cell follicles (B220; in green) and a T cell zone (CD3e; in blue). Scale bar = 100 µm. C) Representative confocal image showing formation of B cell-like structure (B cells isolated from eGFP mice, green) seeded with unlabeled FRC, surrounded by a T cell zone laden (unstained) with TRCs (td-Tomato labeled, red). Dotted line denotes the T-B boundary. Scale bar = 200 µm. Inset i: Close-up of the T-B boundary. D) Representative image of the interface between the extruded B cell-like structure (eGFP; green) and T cell zone (Hoeschst, blue). E) Representative image of extruded B cell follicle (eGFP; green) surrounded by T cell zone laden with TRCs (Td-tomato; red) and T cells (live labeled with Hoechst, blue). Scale bar = 400 µm.

these conduits could be carved into hydrogels with precision and in proximity to desired structural elements, such as B cell follicles (Figure 4D).

Thus, we were able to generate a perfusable hydrogel-based LN model capable of recapitulating key structural and cellular elements including lymphatic vessels, conduits, a stromal compartment, and defined T/B cell zones.

2.4. The eLN Is Able to Generate a Robust Immune Response to Inflammatory Stimuli

Having optimized LN architectural features and constituents, we then tested the capacity of mouse immune cells within the engineered eLN to respond to inflammatory cues delivered via the lymphatic channel, in a manner mimicking drainage of

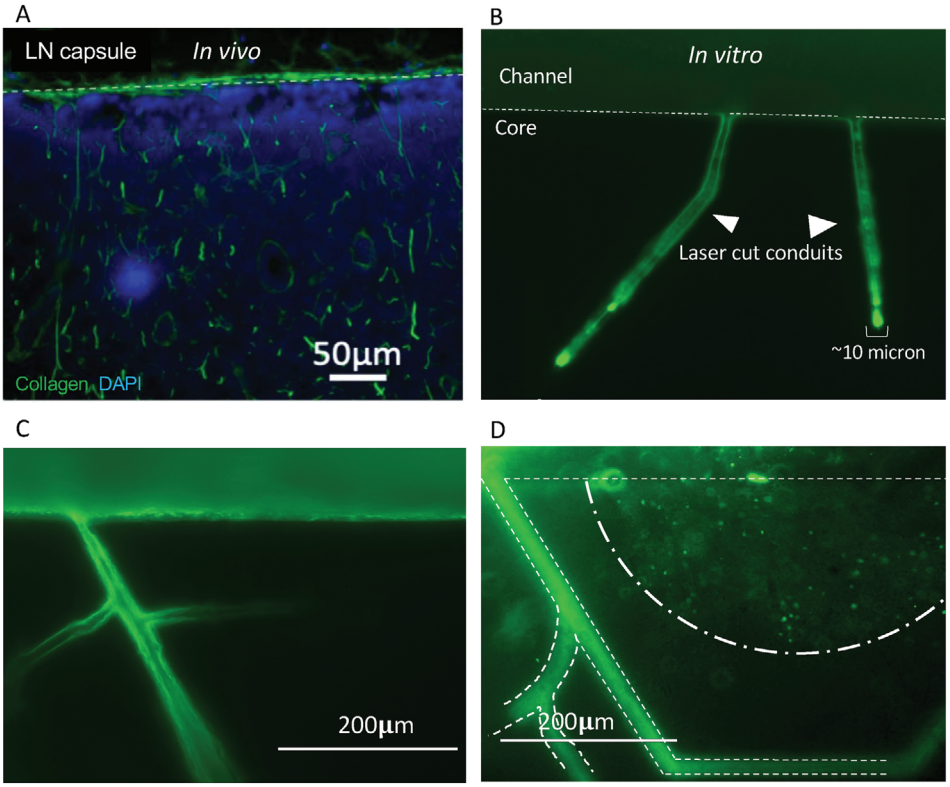

Figure 4. Formation of conduit-like structures to bridge the vessel and cell-laden gel. A) Confocal image of a murine LN section showing the lymph node capsule and conduits extending into the LN paracortex (Collagen I, green; Nuclei, DAPI. Scale bar 50 μm. B) Representative example of laser-carved conduits (10 μm in width) within an acellular gel, stemming from main sinus channel, highlighted by white arrows. 1 μm fluorescent microbeads perfused into channel mark the channel and conduit in green. C) Vessel with branching laser-carved conduit visualized after perfusion of fluorescent microbeads. Scale bar = 200 μm. D) Fluorescent microscopy image showing laser-carved ramifications from a cast channel perfused with 1 μm microbeads (dashed line), extending into a cell-laden gel and adjacent to an extruded B cell follicle-like structure (dash- dot line). Scale bar = 200 μm.

inflammatory factors from peripheral tissues. eLNs were prepared as described above, then a cocktail of PMA and ionomycin was either added to the culture medium to bathe the entire device for 4 h (static) or was perfused through the lymphatic channel for 12 h (**Figure** 5A). Cells were then harvested, and the expression of activation markers on T and B cells was measured using flow cytometry (gating strategy, Figure 5B). In static conditions, PMA/ionomycin stimulation induced a reduction in naive murine $CD4^+$ and $CD8^+$ T cells ($CD44^{lo}CD62L^{hi}$; Figure 5C–F), and a concurrent induction of effector memory cells (EM, $CD44^{hi}CD62L^{lo}$; Figure 5D–G) was observed. Perfusion of PMA/ionomycin via the lymphatic channel induced a strikingly similar response, albeit to a lesser extent (Figure 5C,D,F,G). Unsurprisingly, addition of PMA/ionomycin in both static and flow conditions had little to no effect on the presence of central memory T cells (CM; Figure 5E–H). We then measured CD69 expression (marker of early activation) on the T and B cells to assess the response to PMA/ionomycin stimulation. Again, delivery via the lymphatic channel induced a significant increase in the proportion of $CD69^+$ T and B cells, in a similar manner to the static condition (Figure 5I–K). This was not limited to PMA/ionomycin. Perfusion with LPS also induced an enhancement in CD69 expression by $CD4^+$ T cells, $CD8^+$ T cells and B cells, although responses to LPS were not as potent as PMA/ionomycin (Figure S5, Supporting Information)

Together, these data indicate that delivery of exogenous stimuli solely via the lymphatic channel of eLNs is sufficient to induce a potent inflammatory response reminiscent of infection scenarios where signals are delivered from peripheral tissues.

Having modeled nonspecific sterile inflammation, we then examined the capacity of immune cells within the eLN to respond in an antigen specific manner, following exposure to an antigen. To do this we performed a competition assay within the eLN where the cell-laden core contained both nonspecific T cells from CAG-eGFP mice, and live-labeled OT-I T cells from mice engineered to recognize the antigen ovalbumin (OVA). eLNs were then either bathed (static) or perfused (flow) with PMA or the OVA peptide, $OVA_{257–264}$ (SIINFEKL), before T cell responses were measured (**Figure** 6A). Again, T cells with nonspecific T cell receptors responded to PMA/ionomycin stimulation, showing a significant shift in naive CD8 T cells toward EM T cells. However, these cells did not respond to $OVA_{257–264}$ stimulation (Figure 6A,B–E). OT-I T cells within the same gels responded comparably to nonspecific PMA stimulation, both in static and flow conditions. Interestingly, an equivalent drop in $CD8^+$ naive T cells and rise in EM was detectable (Figure 6B,C). However, in stark contrast to nonspecific $eGFP^+$ T cells, these cells mounted a significant antigen-specific response to $OVA_{257–264}$ stimulation. A profound reduction in the abundance of naive T cells was quantified, with perfused OVA being equally efficient in exerting an

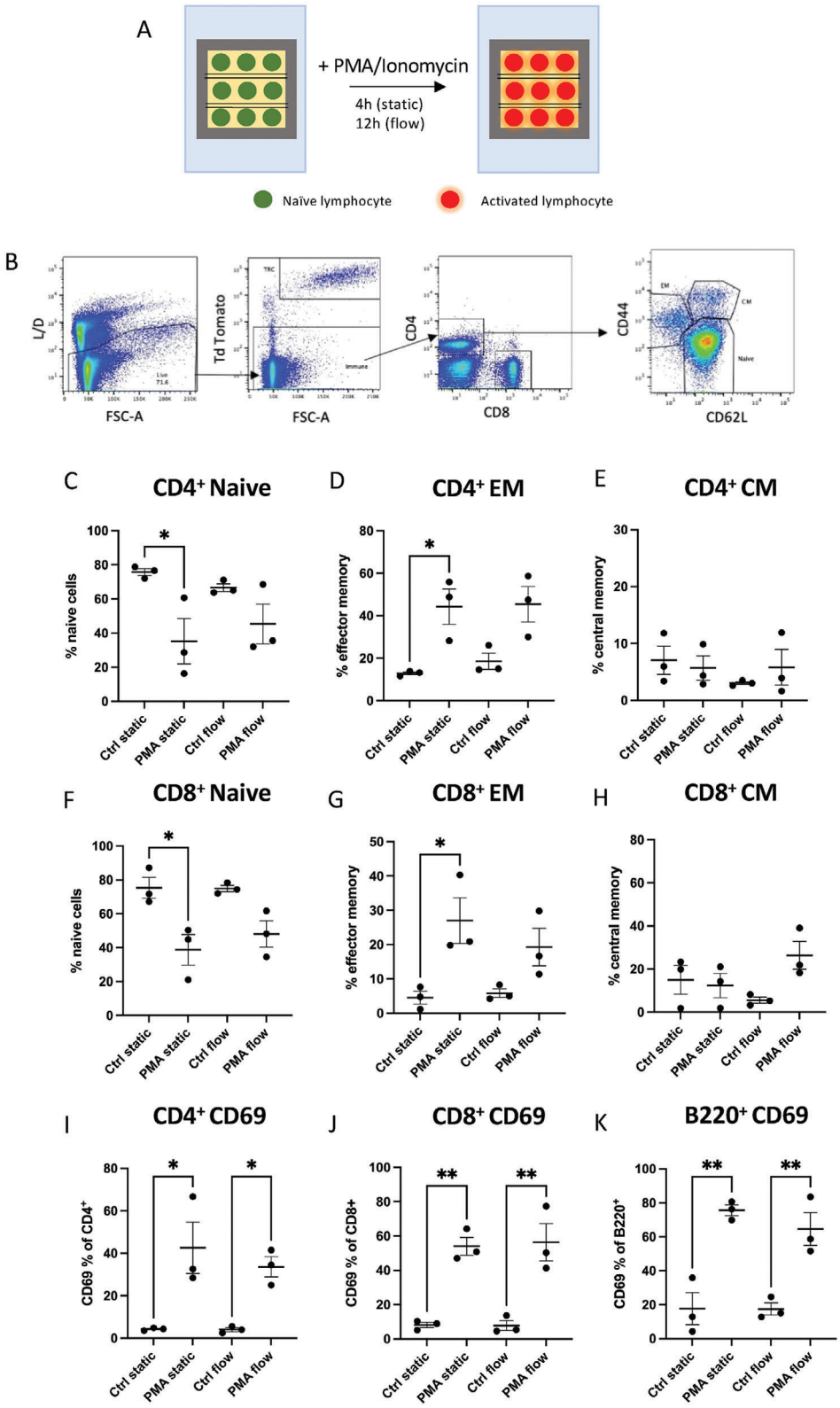

Figure 5. The eLN reacts to perfused PMA/ionomycin stimulation. A) Schematic of PMA/ionomycin activation assay. B) Flow cytometry gating strategy. Flow cytometry quantification showing percentages of naive, EM, and CM among the C–E) $CD4^+$ T cells, F–H) $CD8^+$ T cells, and I–K) CD69 expression on $CD4^+$ T cells, $CD8^+$ T cells and $B220^+$ B cells. Samples were incubated with PMA/ionomycin or normal medium in static or flow culture conditions. Each dot represents independent experiment ($n = 3$). One-way ANOVA and Tukey's multiple comparisons tests were conducted. ns = not significant ($p > 0.05$), *$p \leq 0.05$, **$p \leq 0.01$, ***$p \leq 0.001$, ****$p \leq 0.0001$.

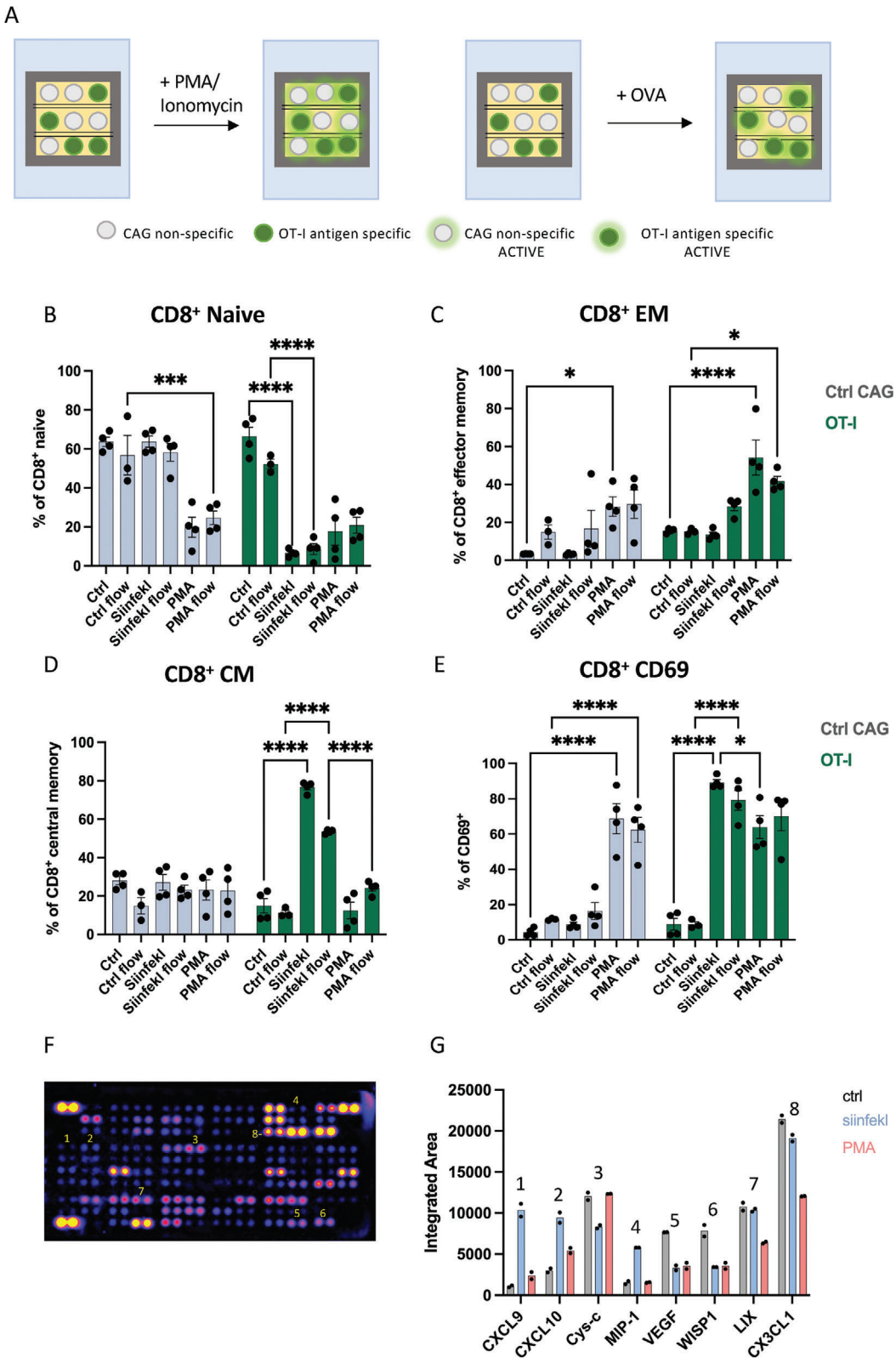

Figure 6. The eLN generates antigen-specific activation in response to perfused stimuli. A) Schematic of the experimental setup. Both OT1 and WT T cells respond to PMA, but only OT1 respond to OVA stimulation. B–E) Flow cytometry quantification of OT-I (in green) and WT (CAG, in gray) $CD8^+$ T cells showing percentages of nave, EM, CM, and $CD69^+$ after stimulation with either control medium, the OVA peptide $OVA_{257–264}$ (SIINFEKL), or PMA/ionomycin (PMA), both in static and flow conditions. Each dot represents independent experiment (at least $n = 3$). Two-way ANOVA and Tukey's

effect. A slight increase in EM was also detected, however, unlike PMA stimulation, a significant increase in CM CD8$^+$ T cells was detected after antigen exposure, albeit to a lesser extent in the perfused system compared to the static (Figure 6D). Moreover, while both PMA/ionomycin and OVA$_{257–264}$ were capable of inducing CD69 expression in OT-I T cells to a similar extent, non-specific CAG-eGFP T cells only responded to PMA/ionomycin (Figure 6E). Measurement of cytokines from harvested perfusate highlighted an OVA-specific increase in CXCL9 and 10 and MIP-1, confirming changes in the secretion profiles of cells within the gel following perfused stimulation (Figure 6F,G and Figure S6, Supporting Information).

As other pathological conditions such as cancer can also influence LN behavior, we finally sought to identify if the eLN may also be used as a surrogate to study tumor-stimulated LN adaptations. We have previously shown that tumors remotely modify the behavior of stromal cells in draining lymph nodes (TDLNs) via delivery of tumor-derived cues.[17,30] In particular, we described that the production of the naive T cell survival cue IL-7 was downregulated in fibroblasts of tumor draining lymph nodes. With this in mind, we collected tumor-conditioned media (TCM) and perfused the eLN for 4 d to simulate the continued drainage occurring between tumors and downstream TDLNs. Measurement of gene expression in murine TRC isolated from the eLN confirmed a similar significant downregulation of IL-7 after perfusion of conditioned medium (Figure S7A,B, Supporting Information), indicating that perfusion of the eLN also allows for evaluation of stromal changes, modeling the tumor condition.

In summary, scenarios known to induce modulation of stromal cells can be modeled in the device, and the response to a wide range of stimuli can be detected both in lymphoid and stromal populations.

3. Discussion

LNs have a tightly regulated, highly organized structure. Coordinated cell migration events and interactions are required for the initiation of robust immune responses.[1,31–33] In this study, we developed an open hydrogel-based eLN that incorporates key structural and cellular elements, is designed to fit on a coverslip for live imaging applications and supports rapid cell isolation for diverse post hoc analyses. The eLN contains primary murine lymphocytes, alongside non-immune FRCs and LEC components to create lymphatic vasculature, conduits, a stromal network, and defined T/B cell zones. Here, the eLN was used to model the effect of flow-delivered inflammatory cues on the generation of an immune response.

Much of our understanding of events within LNs comes from elegant in vivo intravital imaging studies.[34–38] Despite the importance of these studies to understand fundamental LN functions, they remain technically challenging and require specialist microscopy equipment. To circumvent this, a growing number of in vitro systems have been described, with the aim of exploring immune cell biology. To date, their application has been confined to specific aspects of LN and tertiary lymphoid organ biology, such as immune infiltration, SCS function, chemotaxis, immune cell interactions, or germinal center formation and antibody production.[9,39–42] More recently, bioreactor and organoid approaches have been developed to incorporate multiple aspects of the LN but do not yet fully capture the complexity of the LN structure.[43,44]

With this eLN model, we sought to find a hydrogel blend formulation capable of supporting cellular characteristics and providing mechanical stability to sustain the embedded channel lumen. In contrast to other studies using collagen or agarose hydrogels as a scaffold,[39,45,46] we observed that collagen-based gels rapidly contracted and were unable to maintain a perfusable channel. This was likely due to the presence of multiple cell types at a high density, including fibroblasts. As Collagen I represents one of the major ECM component of LNs,[47,48] we therefore optimized a combination of collagen and gelatin-based GelMA to provide the desired properties. This composition allowed the formation of a robust channel structure suitable for endothelial cells, while also enabling embedded cells to adopt elongated morphology and interact with the surrounding collagen fibers without significant degradation or contraction. In the future, additional ECM formulations such as Matrigel or fibronectin could be incorporated to enhance chemokine binding and gradient formation required for effective immune homing.[42,49]

The viability and functionality of immune cells within the eLN was dependent on the presence of FRCs and their secretomes, consistent with their roles in immune survival in vivo.[23,41,50–52] Addition of IL-4 and IL-7 significantly enhanced the viability of immune cells, particularly primary murine B cells, which are known to exhibit low viability in ex vivo models.[21,22] Unlike previous devices which employed immortalized T and B cells,[53,54] the use of primary B cells has the potential to model aspects of humoral immunity including proliferation of naive cells and differentiation to and become antibody secreting cells.[9,55] It should be noted that the process of photo-crosslinking of gelMA has been linked to decreased long-term cell viability,[56] and while the short duration of UV-exposure used here did not impact T cell viability, it is possible that B cells were more susceptible, thus longer term examination of viability and immune functionality is warranted.

Critical to LN function in vivo are the compartmentalization of T and B cells into distinct zones,[57] and conduits that facilitate rapid transit of small molecules and pathogens.[58] To recapitulate this organization, the eLN modeled B cell follicles distributed within T cell rich zones. Their inclusion offers an in vitro platform to a) mechanistically determine how compartmentalization, which is frequently perturbed in infection and TDLNs,[59–61] modulates immunity, and b) screen for agents that restore function. In healthy tissues, a tightly regulated MW cut-off limits conduit access to low MW chemokines and antigen.[29] In infection and

multiple comparisons tests were conducted. ns = not significant ($p > 0.05$), *$p \leq 0.05$, **$p \leq 0.01$, ***$p \leq 0.001$, ****$p \leq 0.0001$. F) Representative cytokine array film. Each doublet of dots represents a different cytokine detected in the medium. Numbers correspond to cytokines highlighted in graph (G). G) Quantification of selected cytokines showing integrated area of fluorescence. The test was performed on media collected from devices following incubation with SIINFEKL (in blue), PMA/ionomycin (in red), or control medium (in gray). Each dot represents technical repeats ($n = 2$).

cancer, however, vessels lining the LN become leakier to impact the selectiveness of transport into the conduits via mechanisms that are currently unclear.[17,62] Thus incorporation of conduit-like structures branching off the main endothelial-lined vessel may provide a valuable tool to understand mechanisms underpinning LN vessel leakiness, transport of molecules into conduits and functional impact of these changes in disease, in real time. It should be noted that although conduit like structures here are larger than in vivo, and MW cut-offs may not be faithfully recapitulated, they offer a route for rapid transport of soluble cues deeper within the cell laden core, as occurs in vivo. To better model conduits and control their width, future work may identify approaches to control parameters for laser carving or devise alternative methods for their creation.

Consistent with other flow devices,[26,63] perfusable, flow responsive cell-lined channels were incorporated into the eLN, modeling the lymphatics. Previous LN-based microfluidic studies,[52,64] including work by Birmingham et al. modeled SCS interactions to reveal that changes to sheer stress modulate cell endothelial receptor repertoires, influencing arrest of perfused THP1 and cancer cells.[41] The eLN shares the ability to investigate mechanisms of endothelial interactions under physiological and pathological settings with different flow rates, but also permits examination of interactions and movement within the eLN post egress.

Beyond immune cells, the stromal compartment is an essential constituent of LN that was incorporated into the eLN.[19,62,65–67] Although immune cells account for >90% of the total LN, increasing evidence has demonstrated the importance of stromal cells in maintaining organ function;[68–72] their modulation or destruction in infection[6,73] and cancer[17,30] can significantly impact LN organization and immune functionality. Indeed, FRCs orchestrate cell migration and survival via secretion of cues such as CCL21 and IL-7,[68,74] factors that are upregulated in inflammation[18,65] but significantly downregulated in tumor draining LNs.[17] Here, we perfused the eLN with tumor-conditioned media to simulate the interaction between tumors and downstream TDLNs, and measured downregulation of FRC-derived IL-7 mirroring previously reported events in vivo.[17] This indicates that the eLN can be used to investigate the impact of diseases such as cancer, dissecting both immune and stromal responses.

We also showed that diverse inflammatory stimuli delivered via the endothelial lined channels efficiently convected into the cell-laden zones to drive immune activation. Both general and antigen-specific responses were measured, alongside cell movement and antigen-specific chemokine induction. Alterations in these may be used as indicators of responsiveness to drugs such as immunotherapies and chemotherapy.[53,75] Thus, as therapeutic agents and tumor-derived factors can rapidly accumulate in LNs, the functional and anatomical properties of the eLN may provide a valuable in vitro platform for mechanistic studies that investigate tumor-induced remodeling, drug or vaccine efficacy and mode of action, and toxicity.[76–79]

4. Conclusion

In conclusion, the eLN model recapitulates key structural and cellular features of murine LNs and exhibits the ability to mount robust immune responses. This engineered eLN model demonstrates promising features and provides a platform for studying murine LN biology and immune responses to diverse stimuli in a tractable system, in real time.

5. Experimental Section

Cell Culture: The B16-F10 murine melanoma cell line was purchased from the American Type Culture Collection (ATCC; Cat: CRL-6475) and maintained in Dulbecco's modified Eagle medium (DMEM) (Gibco, Cat: 11995065) supplemented with 10% v/v fetal bovine serum (FBS; ThermoFisher) and 100 U mL^{-1} penicillin-streptomycin (ThermoFisher) (Full DMEM medium). Fibroblastic reticular cells (FRCs) were isolated from the lymph nodes of $p53^{-/-}$ C57BL/6 mice as previously described.[80,81] The cells were maintained in Roswell Park Memorial Institute formulation 1640 (RPMI-1640) (Gibco, Cat: 21875-034), supplemented with 10% v/v FBS, 1% v/v HEPES buffer (Gibco, Cat: 15630080), 100 U mL^{-1} penicillin-streptomycin, and 15×10^{-6} M β-mercaptoethanol (Sigma) (Full RPMI medium). FRC and T zone fibroblastic reticular cells (TRC) were isolated from lymph nodes of $p53^{-/-}$ C57BL/6 mice as described previously.[82] The isolated TRC fibroblasts (kind gift of Professor Melody Swartz) were transfected with a lentivirus containing a plasmid carrying the Tomato protein and were used for easy detection during live-cell and confocal microscopy as well as in flow cytometry. The cells were maintained in full RPMI medium. C57BL/6 murine primary dermal lymphatic endothelial cells (LECs) were purchased from CellBiologics (Cat No. C57-6064L) and cultured in endothelial cell medium purchased from CellBiologics (Cat No. M1168) supplemented with 10% fetal calf serum (FCS), 1% L-glutamine, 0.1% heparin, 0.1% endothelial growth factor (EGF), 0.1% vascular endothelial growth factor (VEGF), 0.1% endothelial cell growth supplement (ECGS), and 1% antibiotic-antimycotic solution, purchased as a kit from CellBiologics (Cat No. M1168-Kit).

Generation of Conditioned Medium: B16-F10 cells were seeded at a density of 1.5×10^6 cells in T175 cm^2 flasks. The following day the medium was replaced with low serum medium (RPMI-1640 supplemented with 2% FBS, 2% p/s, 10×10^{-3} M HEPES and 15×10^{-6} M β-ME). After 24 h, the medium was harvested, centrifuged at 500*g* for 10 min, to remove cellular debris, and filter-sterilized using SteriFlip vacuum filters (Merck). The medium collected from B16-F10 cells represents TCM. TCM was then aliquoted and stored at −80 °C until use.

Mouse Ethics Statement: All experiments were performed after review and approval by MRC Laboratory of Molecular Biology Animal and Ethical Review Board (AWERB) and approved by the Home Office in accordance with the Animals (Scientific Procedures) Act 1986 and ARRIVE guidelines. Work was performed under authority of Project License P88378375. Adult mice aged between 8 and 12 weeks of age were used for experiments. Animals were socially housed in individually ventilated cages with enrichment.

Mouse Models: All mice were maintained at the MRC Ares Animal Facility (Cambridge, UK). WT C57BL/6 mice were obtained from the in-house breeding facility and used for experimentation. CAG-eGFP mice were purchased from the Jackson Laboratory (Stock No. 003291)—the mice ubiquitously expressed enhanced GFP (eGFP) permitting its use in labeling studies. OT-I mice (C57BL/6-Tg(TcraTcrb)1100Mjb/Crl) were purchased from Charles River. These homozygous mice contain transgenic inserts for mouse Tcra-V2 and Tcrb-V5 genes. The transgenic T cell receptor was designed to recognize ovalbumin residues 257–264 (SIINFEKL) in the context of MHC class I and used to study the role of peptides in positive selection and the response of $CD8^+$ T cells to antigen.

Murine Lymph Node and Spleen Isolation: Spleens and LNs were collected from mice (MRC ARES, Cambridge) and mechanically dissociated using a 25-gauge needle (0.5 mm × 25 mm). Broken tissues were filtered through a 70 µm strainer (Thermo Fisher), using a 1 mL syringe plunger (Soft-Ject), to create a single-cell suspension. Remnant tissues were flushed through with PBS. For splenic tissues, the single-cell suspension was lysed in red blood cell lysis buffer (RBC buffer; 155×10^{-3} M NH4Cl, 12×10^{-3} M $NaHCO_3$, and 0.1×10^{-3} M EDTA in ddH_2O) for

5 min, at room temperature, before neutralization with medium. RBC lysis was not conducted on LN samples. Immune cells were maintained in full RPMI medium containing IL-4 (20 ng mL^{-1}, Peprotech 214-14) and IL-7 (10 ng mL^{-1}, Peprotech 217-17) for the duration of experiments.

MACS Isolation of B220$^+$ B Cells: For B220$^+$ B cell enrichment, spleens were processed into a single-cell suspension. B220$^+$ B cells were isolated using the Pan B cell Isolation Kit II (Miltenyi Biotec, 130-104-443). Isolated cells were counted with a hemocytometer and resuspended at a density of 1×10^8 cells in 400 µL of MACS buffer (0.5% v/v BSA and 2×10^{-3} M EDTA in PBS). 50 µL of Pan B cell Biotin-Antibody Cocktail (Miltenyi Biotec Cat: 130-095-130) was added to the suspension and incubated for 5 min at 4 °C. The cells were resuspended in 100 µL of anti-biotin MicroBeads and 300 µL of MACS buffer and left for 10 min at 4 °C. Magnetic separations were then conducted. The cells were loaded onto a primed LS Column (Miltenyi Biotec, Cat: 130-042-401) attached to a QuadroMACS Separator (Miltenyi Biotec, Cat: 130-091-051). The column was washed with 3 mL of MACS buffer to collect the unlabeled B220$^+$ B cells. Flow cytometry was performed to confirm purity. Viable cells were counted using a hemocytometer and resuspended at the desired concentration for in vitro assays.

Flow Cytometry: Hydrogels were briefly disrupted with a pipette tip and incubated in 2 mg mL^{-1} collagenase A (Roche; COLLA-RO), 2 mg mL^{-1} collagenase D (Roche; COLLD-RO) for 20 min. Once the hydrogel was completely liquified and no particles were visible, the digestion was deactivated using 10×10^{-3} M ethylenediaminetetraacetic acid (EDTA). Samples were then centrifuged at 300 *g* for 5 min, resuspended in sterile PBS, and transferred to round-bottomed 96-well plates (Corning) ready for staining. Cell suspensions were then stained with fixable viability dye live/dead violet (Molecular Probes) and combinations of fluorescently conjugated antibodies (Table S1, Supporting Information). If intracellular epitope detection was required, samples were fixed and stained in accordance with the FoxP3/ Transcription Factor Staining Kit (eBioscience, Cat: 00-5523). Following cellular staining, the samples were run on a LSR Fortessa (BD Biosciences) supported by the FACSDiva program (BD Biosciences). Analysis of data was performed using FlowJo Software.

Cell Sorting for RNA Analysis: For RNA processing, cell sorting was performed on a high-speed Influx Cell Sorter or a FACSAria (100 mmol L^{-1} nozzle, both BD Biosciences) into RLT lysis buffer (QIAGEN, #79216). TRCs were sorted based on signal positivity for TdTomato while B and T cells were separated from the TdTomato negative portion by B220 and CD3 expression. RNA was then isolated with the RNeasy plus micro Kit (QIAGEN, #74034) and RNA quality and quantity was analyzed with a Bioanalyzer (Agilent Technologies). qRT-PCR using 20 ng cDNA input material was performed using TaqMan assays with different primers/probes (Acta2 Mm00725412_s1, Col1a2 Mm00483888_m1, IL-7 Mm01295803_g1, Rns18s Mm03928990_g1). qRT-PCR was performed on a StepOne Real Time PCR System instrument in a relative quantification setting (Life Technologies). Gene expression levels are shown as 2−ddCt.

Collagen Gel Preparation: Rat tail collagen type I was incorporated into hydrogels (Gibco, Warrington, UK). Collagen I gel (final concentration of 2 mg mL^{-1}) was made by mixing collagen I (3 mg mL^{-1}), sourced from rat tail with a solution of 10× PBS (supplemented with 5 µg mL^{-1} phenol red, pH 7.2), and 1 M NaOH (Sigma, Haverhill, UK), while kept on ice. Thermocrosslinking at 37 °C for 30 min allowed the gelation process.

Gelatin Methacryloyl Hydrogel Preparation: Gelatin methacryloyl (GelMA) powder was dissolved in PBS at 60 °C at the desired concentration with the addition of the water soluble photoinitiator lithium phenyl-2,4,6-trimethylbenzoylphosphinate (LAP) at 0.5% w/v. The obtained solution was then aliquoted and stored at −20 °C until use. To crosslink the GelMA solution into a hydrogel, exposure to 405 nm UV light was required. For this study, 20 s was sufficient.

Hydrogel-Based Device with Central Compartment: PLA molds for the device were 3D printed (Ultimaker 3) and used to create polydimethylsiloxane (PDMS) cases for the device. Subsequently, the cases were attached to a coverslip by surfaces plasma cleaning or with silicon glue. 30G sterile stainless steel needles were inserted into side holes incorporated within the design, prior to gel casting. The holes facilitated standardized channel formation and positioning within the device and serve to host tubing inlets and outlets. A magnetic PTFE cube (8 mm × 8 mm × 8 mm) with a steel core was built at the University of Cambridge Department of physics workshop in West Cambridge. The choice of material rendered the cube nonadherent to hydrogels and easily removable with the use of a magnet. To maximize hydrogel adherence to glass coverslips, devices were incubated with 2% polyethyleneimine solution (0 3880, Sigma-Aldrich) at room temperature for 10 min and 0.1% glutaraldehyde solution (G6257, Sigma-Aldrich) at room temperature for 30 min. Before gel loading, devices were washed five times with PBS. After needle insertion, chambers were filled with liquid GelMA and rapidly cross-linked with a handheld 405 nm UV lamp for 10 s. The needles and the cube were then slowly removed to create two hollow structures that were utilized as vessels separated by a central compartment filled with a collagen I gel solution laden with FRCs and lymphoid isolates (Figure S1A,B, Supporting Information).

Hydrogel Blend Device: To create a single material device, a hydrogel composed of both collagen I and GelMA was used. GelMA dry powder (Sigma, Cat No. 900622) was dissolved in PBS to achieve a solution at 10% w/v, while a collagen solution was prepared according to the procedure previously described. The collagen I solution was prepared on ice where it maintains its liquid form. Of note, GelMA naturally undergoes thermal crosslinking below 22.5 °C and was kept at 37 °C. A cell pellet was then resuspended in the GelMA solution. Both GelMA and collagen I solutions were kept at room temperature for 2 min to equilibrate before pipetting the collagen I into the cell-laden GelMA. This ensured an evenly mixed product that was subsequently casted and UV crosslinked into the devices where 26G needles were already in place. The device was then kept in medium at 37 °C overnight until seeding of LECs.

Cell Culture within Devices: All devices were UV sterilized in a sterile biosafety hood before seeding cells. LECs were prepared for seeding into channels at a concentration of 25×10^6 cells mL^{-1}. 5 µL of suspension was slowly perfused on both sides of the channels with a pipette (P10) and the device incubated for at least 2 h to ensure adherence to the bottom of the channel. The device was then flipped 180° and the seeding process repeated for cells to adhere to the opposite side. After 2 h the device was then covered with medium and incubated at 37 °C until LECs formed a monolayer. Media was changed daily. Once channels were confluent, the devices were ready to be perfused with an ultraslow peristaltic pump (Ismatec IPC-N 8). Final concentrations of FRCs and lymphoid cells were 0.4×10^6 cell mL^{-1} and 50×10^6 cells mL^{-1}, respectively, optimized to ensure maximum density to mimic in vivo settings while still allowing optimal imaging.

B Cell Follicle Formation: B cell follicle-like structures were formed in the same GelMA/collagen hydrogel solution. Hydrogel was laden with MACS isolated B220$^+$ cells from CAG.eGFP mice and FRCs at the desired concentrations, loaded into a 1 mL luer lock syringe, and kept at 4 °C for 15 min. This resulted in both gels increasing in viscosity—a property that was utilized to deposit B cell rich spherical shapes in the device by syringe extrusion before filling the rest of the device chamber with a T cells and TRCs-laden solution. Follicles were not UV crosslinked alone to prevent a solid interface with the surrounding gel that would prevent intercompartmental cell interactions and solute movement. The device was then transferred to 37 °C for 2 min before UV light was applied for total crosslinking of all compartments.

Confocal Microscopy: Imaging relied on intrinsic cell fluorescence or prelabeling. TRC and splenocytes from CAG.egfp detectable by Tomato and GFP expression, while cells collected from OT-I or C57BL/6 were live labeled before seeding with Hoechst 33342 (cat: C10337) or CellTrace Far Red Cell stain (cat: C34564). Devices were imaged using either the EVOS Cell Imaging System or Leica Sp5 confocal microscope.

Live-Cell Microscopy: The live-cell imaging experiments were performed with a Zeiss Z1 AxioObserver. Images of cell-laden hydrogels were taken every 10 min to capture lymphocyte movement for a total duration of 24 h.

Scanning Electron Microscopy: Scanning electron microscopy (SEM) was performed on polymerized GelMA (5% and 8%) and GelMA/collagen hydrogels (1 mg mL^{-1} collagen and GelMA 7.5%, 5%, and 4%). Following polymerization, hydrogels were fixed with 4% PFA in PBS for 30 min at room temperature. Then, after three 10 min washes in PBS and two 10 min washes in ddH_2O, hydrogels were transferred into disposable

cryosectioning base molds (ThermoFisher) and stored at −80 °C overnight. Samples were then lyophilized under vacuum with a freeze-drying system (Thermo Savant Modulyo) for 24 h. The specimens were then gold-coated and imaged at 10 kV, magnifications of 500×, 1000×, and 4000×. SEM images were analyzed using NIH ImageJ software. Average pore size was calculated in 500× images, following a diagonal line for each field of view and hand-measuring with a software option. Each SEM image had similar contrast and brightness, as well as the same electron beam voltage. Fiber width was also measured in an analogous manner. Fiber widths were estimated using a line-drawing feature of ImageJ that reports line length in micrometer. Fibers were measured roughly at the midpoint of each fiber; pixels were converted to micrometer measurements using SEM image scale bars.

Second Harmonic Generation: Second harmonic generation acquisition of different hydrogel formulations laden with fluorescent TRCs was performed using a Leica SP5. GelMA-only hydrogels were imaged as a negative control and GelMA/Collagen blends, both at $t = 0$ and after 48 h of TRC 3D culture. Hydrogel samples were collected and transferred to a glass-bottom Petri dish for optimal imaging. A Ti:Sapphire laser (Chameleon Vision 2, Coherent) was used for two-photon fluorescence excitation, with a wavelength of 880 nm. The signal was collected using long working distance objectives (20×/0.40 and 40×/0.80 oil immersion objective (Olympus, Tokyo, Japan)) with a field of view of 110 µm. The SHG signal was obtained using a bandpass filter 435–445 nm.

Conduit Fabrication by Laser Carving: A PALM MicroBeam laser microdissection system (Zeiss) was used to carve perfusable microchannels that stemmed from the main molded channel. Devices were placed in a 35 mm petri dishes without the bottom before transfer to the stage. The generation of microchannels within the hydrogel was achieved using a nanosecond laser system (1-ns pulses, 100-Hz frequency, 355 nm) equipped with a 20×/0.4 NA objective, at a constant stage speed and a laser power. The desired design of the microchannels was drawn via the laser system interface with a line drawing tool. With these settings, carved channels had a diameter of ≈10 µm. To determine accessibility of carved microchannels to perfused solutes, a solution of green fluorescent microbeads mixed in PBS was flowed through channels with a syringe and then imaged.

Dextran Diffusion Assays: Solute transport out of vessels was visualized by dextran diffusion. Lysine fixable Texas Red labeled 70 kDa (cat: D1818), and 3 kDa (FITC) solutions were prepared to final concentrations of 1×10^{-3} M. Dextran solutions were perfused into the acellular channel of the device at a fixed flow rate of 80 µL min^{-1}. Solute transport was recorded by live-cell imaging with time points taken every 5 min over 1.30 h per vessel. After this, perfusion was maintained for 2 h, after which dextran laden gels were fixed with 4% PFA and analyzed by confocal microscopy.

PMA/Ionomycin Activation: Cell-laden hydrogels containing lymphocytes were incubated with 20 ng mL^{-1} PMA (Sigma, Cat No. P1585) and 1 µg mL^{-1} ionomycin (Sigma, Cat No. I0634). The activating solution was provided by either through flow in the channel overnight, or as a 3 h static incubation where the solution covered the cell-laden hydrogels. After the incubation, cells were retrieved from gels, prepared and stained with fluorescently conjugated antibodies (Table S1, Supporting Information) for flow cytometry.

Antigen-Specific Activation: To measure antigen-specific responses, lymphocytes from OT-I mice were isolated and used, mixed in a 1:1 ratio with nonspecific lymphocytes from CAG.egfp mice. The hydrogels were incubated or perfused with 10×10^{-9} M SIINFEKL ($OVA_{257–264}$) overnight for static and flow conditions, respectively. Flow experiments were performed at a fixed flow rate of 80 µL min^{-1}. Hydrogels in devices were then enzymatically digested for cell retrieval, and analysis by flow cytometry.

Cytokine Array: Cytokine arrays were performed according to the R&D System Proteome Profiler Mouse XL Cytokine Array Kit (R&D Systems, #ARY028) product manual. Two milliliters of culture medium from LN 3D cultures laden with OT-I and CAGs in a 1:1 ratio were collected. The gels were differentially treated either with PMA, with SIINFEKL or culture with medium supplemented with IL-7 and IL-4. The medium was centrifuged at 300 *g* to remove cell debris and passed through a 0.2 mm syringe filter. Analysis was performed in ImageJ with the "Protein Array Analyzer" Macro.

Statistical Analysis: Statistical analysis was performed in GraphPad Prism. When comparing two conditions, *T*-tests were used, and when comparing three or more groups a one-way ANOVA and Tukey post hoc test was performed. Data was deemed statistically significant with a *P*-value of <0.05.

Supporting Information

Supporting Information is available from the Wiley Online Library or from the author.

Acknowledgements

The authors would like to thank Andrew Trinh (MRC Cancer Unit) for SHG, Alex Casabuena (Department of Engineering, University of Cambridge) for SEM microscopy, Prof. Melody Swartz for the kind gift of Td-Tomato labeled TRC, The Cambridge Cavendish Laboratory workshop for building the magnetic PTFE cube used in the two-hydrogels device, members of the CIMR flow cytometry core for assistance with flow cytometry applications, and staff at the ARES animal facility for assistance with murine tissues. This work was supported by Medical Research Council Core funding (J.S., H.M., and C.M., Grant No. MC_UU_12022/5), WD Armstrong Foundation (C.M. and I.M.L.), and European Research Council (Y.Y.S.H., Grant No. 758865).

Conflict of Interest

The authors declare no conflict of interest.

Data Availability Statement

The data that support the findings of this study are available from the corresponding author upon reasonable request.

Keywords

compartmentalization, immune activation, lymph node, matrix, perfuse

Received: October 26, 2023
Revised: April 8, 2024
Published online:

[1] U. H. Von Andrian, T. R. Mempel, *Nat. Rev. Immunol.* **2003**, *3*, 867.
[2] A. Link, T. K. Vogt, S. Favre, M. R. Britschgi, H. Acha-Orbea, B. Hinz, J. G. Cyster, S. A. Luther, *Nat. Immunol.* **2007**, *8*, 1255.
[3] M. Bajénoff, J. G. Egen, L. Y. Koo, J. P. Laugier, F. Brau, N. Glaichenhaus, R. N. Germain, *Immunity* **2006**, *25*, 989.
[4] C. Park, I.-Y. Hwang, R. K. Sinha, O. Kamenyeva, M. D. Davis, J. H. Kehrl, *Blood* **2012**, *119*, 978.
[5] C. L. Willard-Mack, *Toxicol. Pathol.* **2006**, *34*, 409.
[6] A. L. St John, S. N. Abraham, *Nat. Med.* **2009**, *15*, 1259.
[7] R. O. Smith, W. B. wood, *J. Exp. Med.* **1949**, *90*, 567.
[8] J. L. Gregory, A. Walter, Y. O. Alexandre, J. L. Hor, R. Liu, J. Z. Ma, S. Devi, N. Tokuda, Y. Owada, L. K. Mackay, G. K. Smyth, W. R. Heath, S. N. Mueller, *Cell Rep.* **2017**, *18*, 406.
[9] G. Goyal, P. Prabhala, G. Mahajan, B. Bausk, T. Gilboa, L. Xie, Y. Zhai, R. Lazarovits, A. Mansour, M. S. Kim, A. Patil, D. Curran, J. M. Long, S. Sharma, A. Junaid, L. Cohen, T. C. Ferrante, O. Levy, R. Prantil-Baun, D. R. Walt, D. E. Ingber, *Adv. Sci.* **2022**, *9*, 2103241.

[10] Y. Shou, S. C. Johnson, Y. J. Quek, X. Li, A. Tay, *Mater Today Bio* **2022**, *14*, 100269.
[11] D. E. Ingber, *Nat. Rev. Genet.* **2022**, *23*, 467.
[12] L. A. Low, C. Mummery, B. R. Berridge, C. P. Austin, D. A. Tagle, *Nat. Rev. Drug Discovery* **2020**, *20*, 345.
[13] T. Ozulumba, A. N. Montalbine, J. E. Ortiz-Cardenas, R. R. Pompano, *Front. Immunol.* **2023**, *14*, 1183286.
[14] A. J. Brain. Kwee, A. Akue, K. E. Sung, *bioRxiv* **2023**, https://doi.org/10.1101/2023.03.21.533042.
[15] Y. O. Alexandre, S. N. Mueller, *Immunol. Rev.* **2018**, *283*, 77.
[16] H. Munir, C. Mazzaglia, J. D. Shields, *Adv. Drug Delivery Rev.* **2020**, *161*, 75.
[17] A. Riedel, D. Shorthouse, L. Haas, B. A. Hall, J. Shields, *Nat. Immunol.* **2016**, *17*, 1118.
[18] A. T. Krishnamurty, S. J. Turley, *Nat. Immunol.* **2020**, *4*, 369.
[19] V. Kumar, D. C. Dasoveanu, S. Chyou, T.-C. Tzeng, C. Rozo, Y. Liang, W. Stohl, Y.-X. Fu, N. H. Ruddle, T. T. Lu, *Immunity* **2015**, *42*, 719.
[20] A. P. Baptista, R. Roozendaal, R. M. Reijmers, J. J. Koning, W. W. Unger, M. Greuter, E. D. Keuning, R. Molenaar, G. Goverse, M. M. S. Sneeboer, J. M. M. den Haan, M. Boes, R. E. Mebius, *Elife* **2014**, *3*, e04433.
[21] M. Howard, S. Kessler, T. Chused, W. E. Paul, *Proc. Natl. Acad. Sci. USA* **1981**, *78*, 5788.
[22] J. Finney, G. Kelsoe, *J. Immunol.* **2021**, *207*, 1478.
[23] J. M. Ayuso, M. M. Gong, M. C. Skala, P. M. Harari, D. J. Beebe, *Adv. Healthcare Mater.* **2020**, *9*, e1900925.
[24] G. Simitian, M. Virumbrales-Muñoz, C. Sánchez-De-Diego, D. J. Beebe, D. Kosoff, *Lab Chip* **2022**, *22*, 3618.
[25] M. M. Gong, K. M. Lugo-Cintron, B. R. White, S. C. Kerr, P. M. Harari, D. J. Beebe, *Biomaterials* **2019**, *214*, 119225.
[26] R. Sfriso, S. Zhang, C. A. Bichsel, O. Steck, A. Despont, O. T. Guenat, R. Rieben, *Sci. Rep.* **2018**, *8*, 5898.
[27] G. V. Reynoso, A. S. Weisberg, J. P. Shannon, D. T. McManus, L. Shores, J. L. Americo, R. V. Stan, J. W. Yewdell, H. D. Hickman, *Nat. Immunol.* **2019**, *20*, 602.
[28] R. Roozendaal, T. R. Mempel, L. A. Pitcher, S. F. Gonzalez, A. Verschoor, R. E. Mebius, U. H. von Andrian, M. C. Carroll, *Immunity* **2009**, *30*, 264.
[29] J. E. Gretz, C. C. Norbury, A. O. Anderson, A. E. I. Proudfoot, S. Shaw, *J. Exp. Med.* **2000**, *192*, 1425.
[30] A. Riedel, M. Helal, L. Pedro, J. J. Swietlik, D. Shorthouse, W. Schmitz, L. Haas, T. Young, A. S. H. da Costa, S. Davidson, P. Bhandare, E. Wolf, B. A. Hall, C. Frezza, T. Oskarsson, J. D. Shields, *Cancer Immunol. Res.* **2022**, *10*, 482.
[31] S. Massberg, P. Schaerli, I. Knezevic-Maramica, M. Köllnberger, N. Tubo, E. A. Moseman, I. V. Huff, T. Junt, A. J. Wagers, I. B. Mazo, U. H. Andrian, *Cell* **2007**, *131*, 994.
[32] J. H. Sung, H. Zhang, E. A. Moseman, D. Alvarez, M. Iannacone, S. E. Henrickson, J. C. Torre, J. R. Groom, A. D. Luster, U. H. Andrian, *Cell* **2012**, *150*, 1249.
[33] S. E. Henrickson, M. Perro, S. M. Loughhead, B. Senman, S. Stutte, M. Quigley, G. Alexe, M. Iannacone, M. P. Flynn, S. Omid, J. L. Jesneck, S. Imam, T. R. Mempel, I. B. Mazo, W. N. Haining, U. H. Andrian, *Immunity* **2013**, *39*, 496.
[34] M. J. Lopez, Y. Seyed-Razavi, T. Yamaguchi, G. Ortiz, V. G. Sendra, D. L. Harris, A. Jamali, P. Hamrah, *Front. Immunol.* **2020**, *11*, 487457.
[35] E. F. J. Meijer, H.-S. Jeong, E. R. Pereira, T. A. Ruggieri, C. Blatter, B. J. Vakoc, T. P. Padera, *Nat. Protoc.* **2017**, *12*, 1513.
[36] C. Sumen, T. R. Mempel, I. B. Mazo, Von Andrian, *Immunity* **2004**, *21*, 315.
[37] U. H. V Andrian, *Microcirculation* **1996**, *3*, 287.
[38] J. L. Hor, R. N. Germain, *Trends Cell Biol.* **2022**, *32*, 406.
[39] A. Shanti, N. Hallfors, G. A. Petroianu, L. Planelles, C. Stefanini, *Front. Pharmacol.* **2021**, *12*, 2132.
[40] M. P. Rosa, N. Gopalakrishnan, H. Ibrahim, M. Haug, Ø. Halaas, *Lab Chip* **2016**, *16*, 3728.
[41] K. G. Birmingham, M. J. O'Melia, S. Bordy, D. Reyes Aguilar, B. El-Reyas, G. Lesinski, S. N. Thomas, *iScience* **2020**, *23*, 101751.
[42] U. Haessler, Y. Kalinin, M. A. Swartz, M. Wu, *Biomed. Microdevices* **2009**, *11*, 827.
[43] C. Giese, C. D. Demmler, R. Ammer, S. Hartmann, A. Lubitz, L. Miller, R. Müller, U. Marx, *Artificial Organs*, Wiley, New York **2006**, Vol. *30*, pp. 803–808.
[44] L. E. Wagar, A. Salahudeen, C. M. Constantz, B. S. Wendel, M. M. Lyons, V. Mallajosyula, L. P. Jatt, J. Z. Adamska, L. K. Blum, N. Gupta, K. J. L. Jackson, F. Yang, K. Röltgen, K. M. Roskin, K. M. Blaine, K. D. Meister, I. N. Ahmad, M. Cortese, E. G. Dora, S. N. Tucker, A. I. Sperling, A. Jain, D. H. Davies, P. L. Felgner, G. B. Hammer, P. S. Kim, W. H. Robinson, S. D. Boyd, C. J. Kuo, M. M. Davis, *Nat. Med.* **2021**, *27*, 125.
[45] T. Kraus, A. Lubitz, U. Schließer, C. Giese, J. Reuschel, R. Brecht, J. Engert, G. Winter, *J. Pharm. Sci.* **2019**, *108*, 2358.
[46] L. Radke, G. Sandig, A. Lubitz, U. Schließer, H. H. von Horsten, V. Blanchard, K. Keil, V. Sandig, C. Giese, M. Hummel, S. Hinderlich, M. Frohme, *Bioengineering* **2017**, *4*, 70.
[47] E. P. Kaldjian, J. Elizabeth Gretz, A. O. Anderson, Y. Shi, S. Shaw, *Int. Immunol.* **2001**, *13*, 1243.
[48] H. Wiig, D. Keskin, R. Kalluri, *Matrix Biol.* **2010**, *29*, 645.
[49] F. Lin, E. C. Butcher, *Lab Chip* **2006**, *6*, 1462.
[50] M. Chung, J. Ahn, K. Son, S. Kim, N. L. Jeon, *Adv. Healthcare Mater.* **2017**, *6*, 1700196.
[51] X. Wang, Q. Sun, J. Pei, *Micromachines* **2018**, *9*, 493.
[52] M. M. Gong, K. M. Lugo-Cintron, B. R. White, S. C. Kerr, P. M. Harari, D. J. Beebe, *Biomaterials* **2019**, *214*, 119225.
[53] N. Hallfors, A. Shanti, J. Sapudom, J. Teo, G. Petroianu, S. Lee, L. Planelles, C. Stefanini, *Bioengineering* **2021**, *8*, 19.
[54] A. Shanti, B. Samara, A. Abdullah, N. Hallfors, D. Accoto, J. Sapudom, A. Alatoom, J. Teo, S. Danti, C. Stefanini, *Pharmaceutics* **2020**, *12*, 464.
[55] M. V. J. Braham, R. S. van Binnendijk, A. M. Buisman, R. E. Mebius, J. de Wit, C. A. C. M. van El, *iScience* **2023**, *26*, 105741.
[56] Z. Jiang, K. Jiang, R. McBride, J. S. Oakey, *Biomed. Mater.* **2018**, *13*, 065012.
[57] S. M. Grant, M. Lou, L. Yao, R. N. Germain, A. J. Radtke, *J. Cell Sci.* **2020**, *133*, 133.
[58] M. Sixt, N. Kanazawa, M. Selg, T. Samson, G. Roos, D. P. Reinhardt, R. Pabst, M. B. Lutz, L. Sorokin, *Immunity* **2005**, *22*, 19.
[59] V. Cremasco, M. C. Woodruff, L. Onder, J. Cupovic, J. M. Nieves-Bonilla, F. A. Schildberg, J. Chang, F. Cremasco, C. J. Harvey, K. Wucherpfennig, B. Ludewig, M. C. Carroll, S. J. Turley, *Nat. Immunol.* **2014**, *15*, 973.
[60] S. M. Soudja, S. Henri, M. Mello, L. Chasson, A. Mas, *PLoS One* **2011**, *6*, e22639.
[61] J. van Grevenynghe, R. Halwani, N. Chomont, P. Ancuta, Y. Peretz, A. Tanel, F. A. Procopio, Y. shi, E. A. Said, E. K. Haddad, R. P. Sekaly, *Semin. Immunol.* **2008**, *20*, 196.
[62] V. G. Martinez, V. Pankova, L. Krasny, T. Singh, S. Makris, I. J. White, A. C. Benjamin, S. Dertschnig, H. L. Horsnell, J. Kriston-Vizi, J. J. Burden, P. H. Huang, C. J. Tape, S. E. Acton, *Cell Rep.* **2019**, *29*, 2810.
[63] A.-C. Vion, T. Perovic, C. Petit, I. Hollfinger, E. Bartels-Klein, E. Frampton, E. Gordon, L. Claesson-Welsh, H. Gerhardt, *Front. Physiol.* **2021**, *11*, 623769.
[64] J. M. Ayuso, M. M. Gong, M. C. Skala, P. M. Harari, D. J. Beebe, *Adv. Healthcare Mater.* **2020**, *9*, 1900925.
[65] D. Malhotra, A. L. Fletcher, J. Astarita, V. Lukacs-Kornek, P. Tayalia, S. F. Gonzalez, K. G. Elpek, S. K. Chang, K. Knoblich, M. E. Hemler, M. B. Brenner, M. C. Carroll, D. J. Mooney, S. J. Turley, *Nat. Immunol.* **2012**, *13*, 499.

[66] L. Knop, K. Deiser, U. Bank, A. Witte, J. Mohr, L. Philipsen, H. J. Fehling, A. J. Müller, U. Kalinke, T. Schüler, *Eur. J. Immunol.* **2020**, *50*, 846.
[67] G. R. Thierry, M. Kuka, M. De Giovanni, I. Mondor, N. Brouilly, M. Iannacone, M. Bajénoff, *J. Exp. Med.* **2018**, *215*, 2972.
[68] T. Katakai, *Int. Immunol.* **2004**, *16*, 1133.
[69] N. Okamoto, R. Chihara, C. Shimizu, S. Nishimoto, T. Watanabe, *J. Clin. Invest.* **2007**, *117*, 997.
[70] C. Gago da Graça, L. G. M. van Baarsen, R. E. Mebius, *J. Immunol.* **2021**, *206*, 273.
[71] S. Asam, S. Nayar, D. Gardner, F. Barone, *Immunol. Rev.* **2021**, *302*, 184.
[72] Y. Kobayashi, T. Watanabe, *Front. Immunol.* **2016**, *7*, 316.
[73] S. N. Mueller, M. Matloubian, D. M. Clemens, A. H. Sharpe, G. J. Freeman, S. Gangappa, C. P. Larsen, R. Ahmed, *Proc. Natl. Acad. Sci. USA* **2007**, *104*, 15430.
[74] M. Bajénoff, J. G. Egen, L. Y. Koo, J. P. Laugier, F. Brau, N. Glaichenhaus, R. N. Germain, *Immunity* **2006**, *25*, 989.
[75] R. N. Germain, E. A. Robey, M. D. Cahalan, *Science* **2012**, *336*, 1676.
[76] Y. Ding, Z. Li, A. Jaklenec, Q. Hu, *Adv. Drug Delivery Rev.* **2021**, *179*, 113914.
[77] J. Chen, L. Wang, Q. Yao, R. Ling, K. Li, H. Wang, *Breast Cancer Res.* **2004**, *6*, R474.
[78] M. F. C. M. van den Hout, B. D. Koster, B. J. R. Sluijter, B. G. Molenkamp, R. van de Ven, A. J. M. van den Eertwegh, R. J. Scheper, P. A. M. van Leeuwen, M. P. van den Tol, T. D. de Gruijl, *Cancer Immunol. Res.* **2017**, *5*, 969.
[79] A. Muchowicz, M. Wachowska, J. Stachura, K. Tonecka, M. Gabrysiak, D. Wolosz, Z. Pilch, W. W. Kilarski, L. Boon, T. J. Klaus, J. Golab, *Eur. J. Cancer* **2017**, *83*, 19.
[80] A. L. Fletcher, V. Lukacs-Kornek, E. D. Reynoso, S. E. Pinner, A. Bellemare-Pelletier, M. S. Curry, A.-R. Collier, R. L. Boyd, S. J. Turley, *J. Exp. Med.* **2010**, *207*, 689.
[81] S. Hirosue, E. Vokali, V. R. Raghavan, M. Rincon-Restrepo, A. W. Lund, P. Corthésy-Henrioud, F. Capotosti, C. H. Winter, S. Hugues, M. A. Swartz, *J. Immunol.* **2014**, *192*, 5002.
[82] A. A. Tomei, S. Siegert, M. R. Britschgi, S. A. Luther, M. A. Swartz, *J. Immunol.* **2009**, *183*, 4273.